RESEARCH ARTICLE

Ligand-induced growth and compaction of CD36 nanoclusters enriched in Fyn induces Fyn signaling

John Maringa Githaka[1], Anthony R. Vega[2], Michelle A. Baird[3], Michael W. Davidson[3,†], Khuloud Jaqaman[2,*] and Nicolas Touret[1,*]

ABSTRACT

Nanoclustering is an emerging organizational principle for membrane-associated proteins. The functional consequences of nanoclustering for receptor signaling remain largely unknown. Here, we applied quantitative multi-channel high- and super-resolution imaging to analyze the endothelial cell surface receptor CD36, the clustering of which upon binding to multivalent ligands, such as the anti-angiogenic factor thrombospondin-1 (TSP-1), is thought to be crucial for signaling. We found that a substantial fraction of unligated CD36 exists in nanoclusters, which not only promote TSP-1 binding but are also enriched with the downstream effector Fyn. Exposure to multivalent ligands (TSP-1 or anti-CD36 IgM) that result in larger and denser CD36 clusters activates Fyn. Conversely, pharmacological perturbations that prevent the enhancement of CD36 clustering by TSP-1 abrogate Fyn activation. In both cases, there is no detectable change in Fyn enrichment at CD36 nanoclusters. These observations reveal a crucial role for the basal organization of a receptor into nanoclusters that are enriched with the signal-transducing downstream effectors of that receptor, such that enhancement of clustering by multivalent ligands is necessary and sufficient to activate the downstream effector without the need for its de novo recruitment.

KEY WORDS: CD36, Receptor and membrane biology, Signal transduction, Src-family kinase, Super-resolution microscopy

INTRODUCTION

Nanoclustering, whereby membrane-associated proteins exist in metastable nanoscale clusters, is emerging as a prominent feature of plasma membrane organization (Garcia-Parajo et al., 2014). This organization is mediated by lipid–lipid, lipid–protein and protein–protein interactions within the membrane (Simons and Gerl, 2010), and by membrane–cortical-cytoskeleton interactions (Jaqaman and Grinstein, 2012; Mattila et al., 2016; Morone et al., 2006). Much remains to be determined about the nature of nanoclustering, the mechanisms leading to it and its consequences for receptor signaling (Garcia-Parajo et al., 2014).

CD36 is a receptor that is expressed in various cell types (Hoosdally et al., 2009; Silverstein and Febbraio, 2009). In human microvascular endothelial cells (HMVECs), its ligand

[1]Department of Biochemistry, University of Alberta, Edmonton, Alberta, T6G 2H7, Canada. [2]Department of Biophysics, University of Texas Southwestern Medical Center, Dallas, TX, 75390, USA. [3]National High Magnetic Field Laboratory and Department of Biological Science, Florida State University, Tallahassee, FL, 32306, USA.
[†]Deceased

*Authors for correspondence (khuloud.jaqaman@utsouthwestern.edu; touret@ualberta.ca)
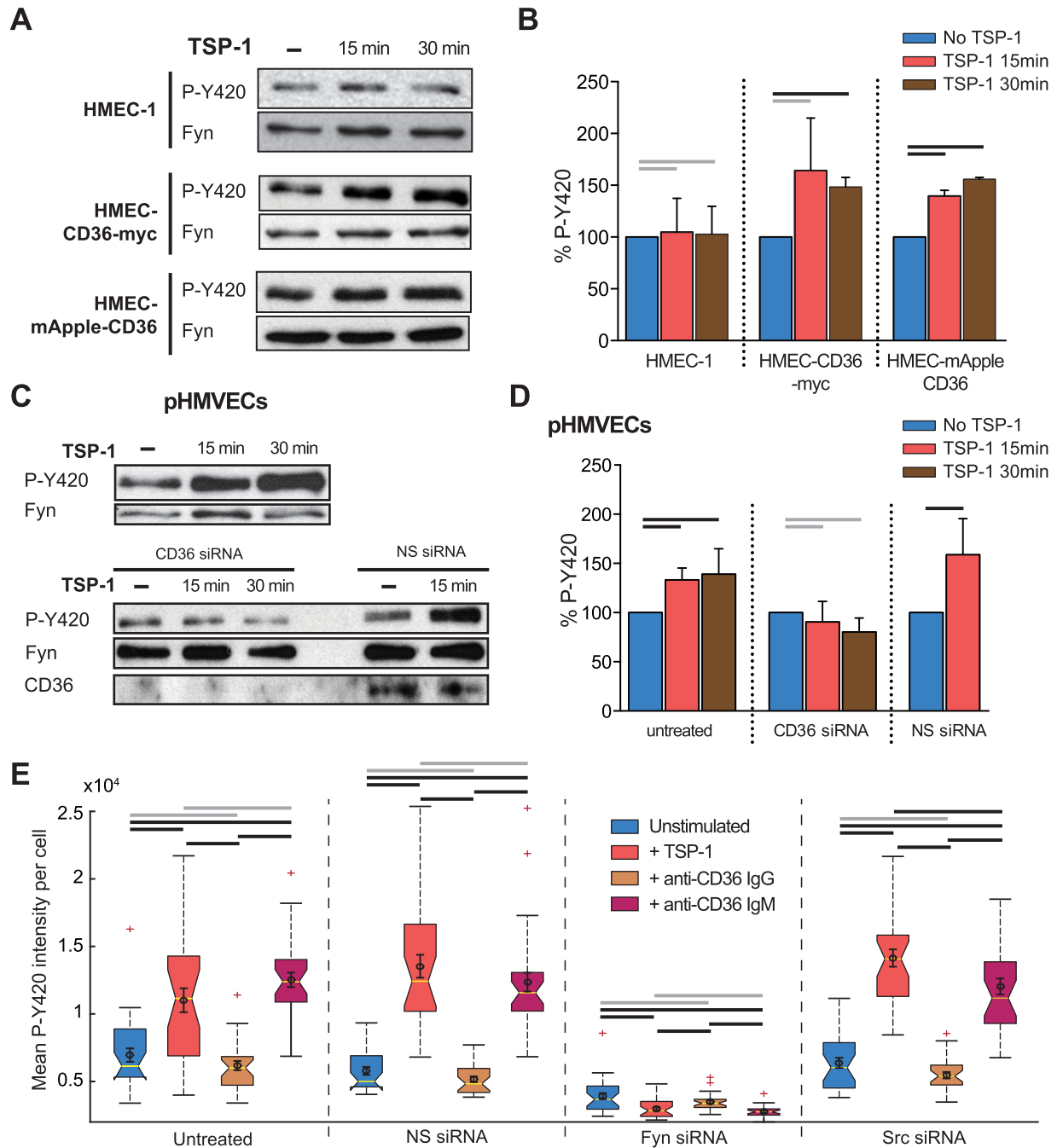
K.J., 0000-0003-3471-1911; N.T., 0000-0003-3700-6302

thrombospondin-1 (TSP-1) is an anti-angiogenic factor; TSP-1–CD36 binding activates the Src-family kinase (SFK) Fyn, leading to caspase-3 activation and apoptosis (Dawson et al., 1997; Jiménez et al., 2000; Volpert et al., 2002). TSP-1 is a trimer, with each monomer containing three 'thrombospondin type-1 repeats' that are responsible for binding to CD36 (Adams and Lawler, 2011; Klenotic et al., 2013). Decavalent anti-CD36 IgM activates Fyn and induces HMVEC apoptosis like TSP-1, whereas bivalent IgG does not (Dawson et al., 1997; Jiménez et al., 2000). This leads to the hypothesis that CD36 clustering by multivalent ligands is crucial for Fyn activation and downstream signaling.

To test this hypothesis and to determine what aspects of nanoclustering influence TSP-1–CD36–Fyn signaling, we explored the nature of CD36 clustering in HMVECs, at basal level and upon ligation. Because the cytoskeleton regulates CD36 dynamics and clustering in macrophages (Jaqaman et al., 2011), we investigated which cellular factors regulate CD36 nanoclustering in HMVECs. We employed photoactivated localization microscopy (PALM) (Betzig et al., 2006) combined with spatial pattern analysis (SPA) (Owen et al., 2010), and conventional total internal reflection fluorescence microscopy (TIRFM) (Fish, 2009) combined with a novel colocalization analysis.

RESULTS

CD36 expression in an immortalized HMVEC line recapitulates TSP-1–CD36–Fyn signaling

To determine CD36 organization with high-spatial resolution, we employed PALM using photoactivatable fluorescent proteins (Lillemeier et al., 2010; Williamson et al., 2011). Photoactivatable fluorescent proteins offer two advantages compared to immunolabeling with organic dyes – they do not 'blink' as much (Dempsey et al., 2011) and each CD36 molecule is fused to only one photoactivatable fluorescent protein. However, PALM requires heterologous expression of CD36. To address this issue, we sought a HMVEC line that expresses little CD36, to which we added CD36 under the control of a weak promoter.

We found that the immortalized line HMEC-1 (Ades et al., 1992) expresses little CD36 (Fig. S1A–C). We used a Moloney murine leukemia retroviral transduction system to establish HMEC-1-based cell lines that stably express CD36–Myc (HMEC-CD36–Myc), mApple–CD36 (HMEC-mApple–CD36) or PAmCherry–CD36 (HMEC-PAmCherry–CD36) (Fig. S1A) under the control of the long terminal repeat of the viral transduction system. The fluorescent proteins were fused to the N-terminus of CD36, as this region is not implicated in signaling (Primo et al., 2005). Comparison of the engineered HMEC lines to primary HMVECs (pHMVECs) by using flow cytometry revealed comparable CD36 expression levels, with a maximum twofold overexpression (Fig. S1B,C). This ensured that our engineered cells did not bias our measurements as a result of overexpression.

Fig. 1. CD36 expression in an immortalized endothelial cell line recapitulates TSP-1–CD36–Fyn signaling. (A) Fyn activation in the indicated HMEC cell lines was probed using anti-P-Y420 immunoblotting, with total Fyn as loading control. All blots (throughout figures) are representative of three independent experiments each. (B) Percentage of P-Y420 in HMEC cell lines quantified as the ratio of P-Y420 to total Fyn intensities from blots, as those shown in A, and normalized to values from untreated cells. Error bars (in all panels) show s.d. Pair-wise comparison *P*-values obtained using Student's *t*-test: black and gray lines indicate *P*-values of <0.05 and >0.05, respectively. (C) Fyn activation in pHMVECs that had been treated with an siRNA against CD36 or a non-specific (NS) siRNA, probed as shown in A. (D) The percentage of P-Y420 in pHMVECs was quantified as described in B. Pair-wise comparison is represented by gray and black lines, as in B. (E) Distribution of the average P-Y420 intensity levels per cell in HMEC-mApple–CD36 cells that had been treated or not with non-specific, Fyn or Src siRNAs, and incubated or not for 10 min with TSP-1 (10 nM), anti-CD36 IgG (FA6-152, 10 µg/ml) or anti-CD36 IgM (SMφ, 10 µg/ml). TIRFM images were acquired, cell areas were segmented, and the mean P-Y420 intensity per cell was measured. Data are from ∼30 cells imaged in three independent experiments. For each box, the yellow central mark is the median, the edges of the box are the 25th and 75th percentiles, the dashed whiskers extend to the most extreme data points not designated as 'outliers', and 'outliers' are plotted individually as red daggers. The notches emanating from the medians are indicative of the 95% confidence interval around the median, shown for visual aid. The overlaid black circle and error bars are the mean and s.e.m. Black and gray lines indicate significantly and not significantly different median values, respectively, using the following two-step statistical testing procedure: first, the Kruskal–Wallis test was used to detect if any median in the group was different from the rest (significance threshold of 0.05). Second, if the Kruskal–Wallis test indicated significant differences, the Wilcoxon rank-sum test was used to perform pair-wise comparisons of the medians between all conditions. Pairs were deemed significantly different if their *P*-value was below the significance threshold, which was calculated using the Dunn–Sidak correction to give a total group type-I error rate of 0.05 (for six comparisons, significance threshold=0.0085 for each comparison).

To verify that the fluorescent protein fusions were functional, we tested whether TSP-1 binding to CD36 activated the SFK Fyn in the engineered cells as it did in pHMVECs. Immunoblotting for phosphorylated SFKs [at residue Y420 (P-Y420); indicative of activation (Saito et al., 2010)] after stimulation with 10 nM TSP-1 (Jiménez et al., 2000) revealed that this was indeed the case (Fig. 1A–D). At the same time, small interfering (si)RNA-mediated depletion of CD36 in pHMVECs (reducing protein levels by >95%; Fig. 1C) abrogated TSP-1 binding (Fig. S1D,E) and SFK activation (Fig. 1C,D), resulting in similar levels of Fyn activation to those in HMEC-1 cells, which lack CD36 (Fig. 1A,B). These experiments confirmed that our CD36 fusion proteins were functional and that, consistent with previous studies (Jiménez et al., 2000), Fyn activation by TSP-1 depends on CD36.

To verify that the increased P-Y420 signal indeed indicated Fyn activation (Jiménez et al., 2000), we used RNA interference (RNAi)-mediated depletion of Fyn or Src. siRNA targeting Fyn (Fyn siRNA) depleted ~80% of Fyn and ~35% of Src; siRNA targeting Src (Src siRNA) depleted ~80% of Src and ~50% of Fyn (Fig. S1F,G). Nevertheless, Fyn-siRNA-treated cells showed no SFK activation upon treatment with TSP-1 (10 nM for 10 min; used from here onwards unless indicated otherwise), whereas Src-siRNA-treated cells were unperturbed, as assessed by immunofluorescence imaging of P-Y420 (Fig. 1E). Therefore, our results confirm that TSP-1 binding to CD36 predominantly activates Fyn. Moreover, decavalent anti-CD36 IgM (SMφ 10 µg/ml for 10 min) activated Fyn in the same manner as TSP-1, whereas bivalent IgG (FA6-152; 10 µg/ml for 10 min) did not (Fig. 1E), consistent with previous reports (Jiménez et al., 2000). These data established our engineered CD36-expressing HMEC lines as faithful model systems in which to study TSP-1–CD36–Fyn signaling.

CD36 is clustered when unligated, and TSP-1 leads to larger and denser clusters

Using the engineered HMEC-PAmCherry–CD36 cells, we determined CD36 nanoscale organization in the absence and presence of TSP-1 by performing PALM. Following treatment with or without TSP-1, cells were fixed and imaged by performing TIRFM (Fig. 2A,B). Fiducial markers were used to correct for lateral drift during imaging (Fig. 2A, arrows). Single-molecule localization (with an average precision of 15–20 nm) and compensation for multiple appearances of a molecule were accomplished using Gaussian-mixture-model fitting and particle tracking (Jaqaman et al., 2008) (see Materials and Methods; Fig. S2A,B). Image and localization quality were very similar between all conditions (Fig. S2B), allowing us to compare CD36 organization between them, although PALM analysis does not yield absolute numbers of molecules (Puchner et al., 2013).

Our experiments revealed that the spatial distribution of CD36 on the ventral cell surface was non-uniform, with seemingly increased clustering upon TSP-1 treatment (Fig. 2B). They also revealed an increase in CD36 surface density upon TSP-1 treatment (Fig. 2C). This increase was reminiscent of vesicle delivery during T-cell receptor signaling (Soares et al., 2013; Williamson et al., 2011), which could play a role in enhancing receptor clustering (Tang and Edidin, 2001). Therefore, we tested whether increased CD36 exocytosis was responsible for the observed increase in CD36 density. However, pulse–chase analysis of CD36 endocytosis and exocytosis (see Materials and Methods) indicated that the increase in CD36 density was due to reduced endocytosis, not elevated exocytosis (Fig. 2D). Therefore, any observed changes in CD36 clustering upon ligation were most likely to be directly induced by ligand.

To identify CD36 clusters and characterize their properties in the absence or presence of TSP-1, receptor coordinates were analyzed by performing SPA (Owen et al., 2010; Williamson et al., 2011), to which we added a randomization-based cluster thresholding scheme (yielding cluster properties with >95% accuracy; Fig. S2C–F; see Materials and Methods). This analysis revealed that, at rest, ~40% of cell surface CD36 molecules resided in clusters, with a median cluster radius of ~70 nm, a molecule density of ~4000 molecules/µm^2 (11-fold higher than the density outside of clusters) and ~75 receptor molecules per cluster (Fig. 2E–K). Upon TSP-1 addition, the fraction of CD36 molecules in clusters increased to ~60%, with the median cluster radius and molecule density inside clusters increasing, and the receptor density outside of clusters decreasing (Fig. 2E–K). The number of CD36 clusters per surface area remained constant (Fig. 2I). These data revealed that a substantial fraction of CD36 exists in nanoclusters at rest and that TSP-1 enhances CD36 clustering, where a larger fraction of CD36 molecules form larger and denser clusters.

CD36 clusters in F-actin-rich regions are equally enriched with Fyn in the absence and presence of TSP-1

Next we used two-color PALM analysis of HMEC-PAmCherry–CD36 cells that had been transiently transfected with Fyn fused to photoactivatable GFP (PAGFP) to investigate when the downstream effector Fyn is recruited to CD36 nanoclusters (Fig. 3A). Fyn and CD36 coordinates were aligned using fiduciary markers. Visually, the Fyn and CD36 spatial patterns did not resemble each other. This was not surprising given that Fyn acts downstream of multiple receptors in various signaling pathways. Therefore, to analyze their location relative to each other, we used SPA to identify CD36 clusters (as above) and cell surface areas with higher-than-average densities of Fyn (Fig. 3B). High-Fyn-density areas covered, on average, 30–35% of the cell surface, contained 70–75% of Fyn molecules at the plasma membrane and were ~fivefold denser with respect to their Fyn content than their surroundings, in the absence and presence of TSP-1 (Fig. 3C–F).

To assess the extent of CD36–Fyn colocalization, we then calculated the fraction of CD36 clusters that coincided with areas of high Fyn density, which we found to be significantly higher than would be expected by chance, both in the absence and presence of TSP-1 (Fig. 3G). The 'by-chance' fraction was calculated by randomizing CD36 cluster positions [as expected, it was equal to the cell surface fraction covered by high-Fyn-density areas (Fig. 3C,G)]. There was no increase in the fraction of CD36 clusters in areas of high Fyn density upon TSP-1 addition (Fig. 3G). There was also no increase in Fyn density at the specific locations of CD36 nanoclusters (Fig. 3H). These data suggest that Fyn was equally enriched at CD36 nanoclusters at all times, without additional recruitment upon TSP-1 binding.

The spatial pattern of Fyn on the membrane was reminiscent of that of the actin cytoskeleton (Fig. 3A). Therefore, to gain further insight into Fyn enrichment at CD36 nanoclusters, we analyzed it in the context of the actin cytoskeleton. We turned to conventional TIRFM imaging of CD36, Fyn and actin simultaneously, as PALM analysis of three molecular species is challenging. HMEC-mApple–CD36 cells were transiently transfected with Fyn–mEmerald, incubated with or without TSP-1 for 10 min, then fixed, permeabilized and stained with phalloidin–Alexa-Fluor-647 (Fig. S3A). Because CD36 nanoclusters were below the diffraction limit (Fig. 2F), they appeared in conventional TIRFM images as diffraction-limited spots. We detected these spots using Gaussian-mixture-model fitting (Jaqaman et al., 2008) and
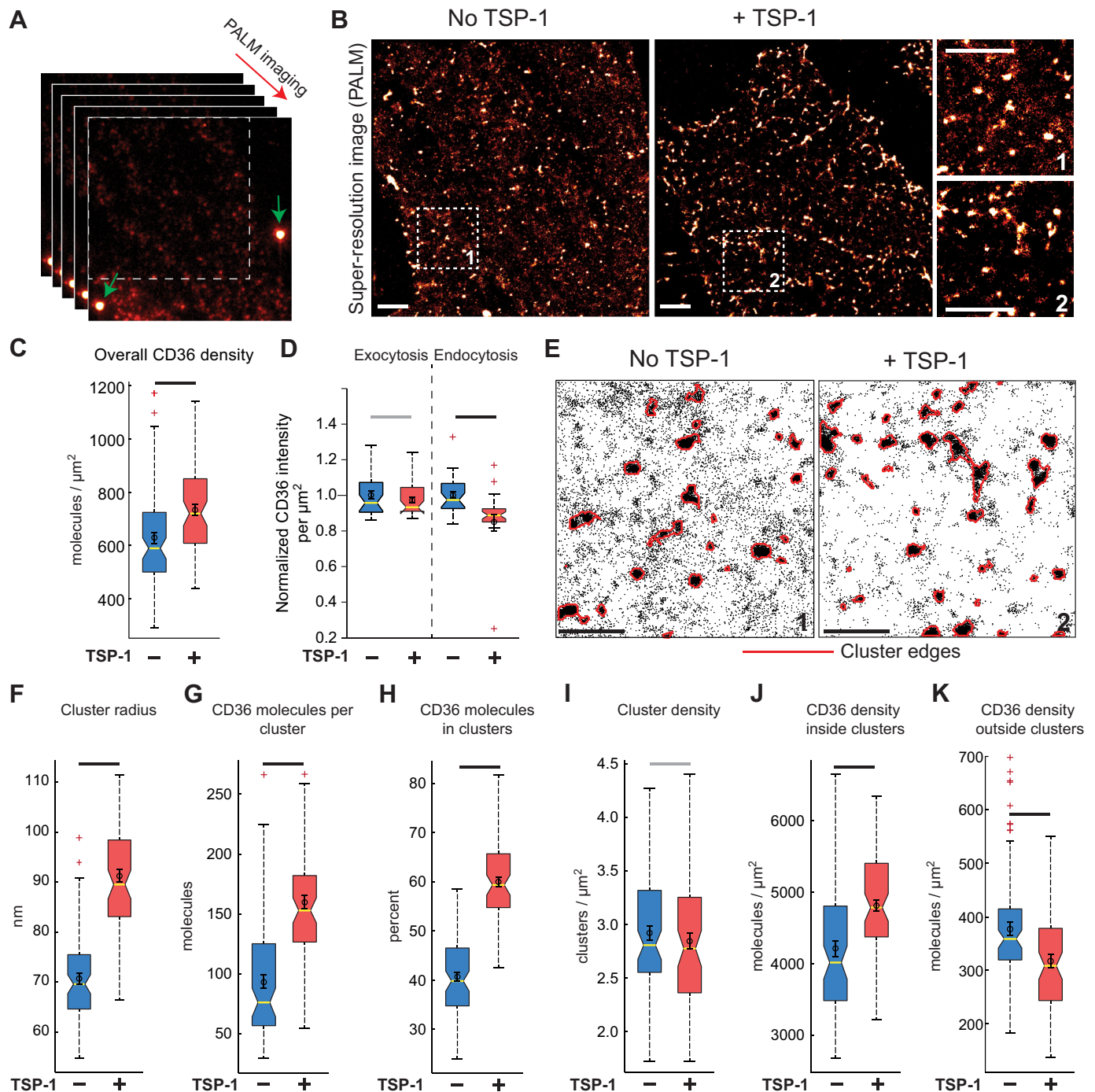
Fig. 2. CD36 is clustered when unligated, and TSP-1 leads to larger and denser clusters. (A) PALM image sequences acquired by TIRFM. Green arrows indicate fiducial markers. (B) PALM images of HMEC-PAmCherry–CD36 cells incubated with or without TSP-1. Insets, zoom-in areas from the corresponding ROIs. Scale bars: 2 µm. (C) Overall density of cell surface CD36. Data from 81 and 70 4×4 µm² ROIs in −TSP-1 and +TSP-1 cases, respectively. Boxplots and statistical tests are as described in Fig. 1E. Data are from three independent experiments, each containing 7–10 different cells. (D) Normalized average intensity of exocytosed or endocytosed CD36 during a 10-min incubation with or without 10 nM TSP-1. Data from ~33 fields from three independent experiments. Boxplots and statistical tests are as described in C. (E) Plots of CD36 molecular coordinates from ROIs 1 and 2 shown in B, with cluster edges, determined by SPA, outlined in red. Scale bars: 1 µm. (F–K) Cluster radius (F), number of CD36 molecules per cluster (G), percentage of cell surface CD36 molecules that exist in clusters (H), number of CD36 clusters per µm² (I), and density of CD36 molecules inside (J) or outside of (K) clusters, from the same ROIs as those shown in C. Boxplots and statistical tests are as described in C.

calculated the enrichment of Fyn, actin or of CD36 itself within them. Briefly, enrichment of species X (X=Fyn, actin or CD36) was defined for each cluster as: (mean intensity of X inside the CD36 cluster)/(mean intensity of X outside CD36 clusters)–1, and then converted to a percentage (Materials and Methods). This addressed

the challenge that the CD36 images were punctate whereas the Fyn and actin images were continuous, for which there is no standard colocalization analysis. With this, we calculated for every detected CD36 cluster (i) its extent of clustering, reflected by the CD36 enrichment value; (ii) whether it was located in an F-actin-rich or
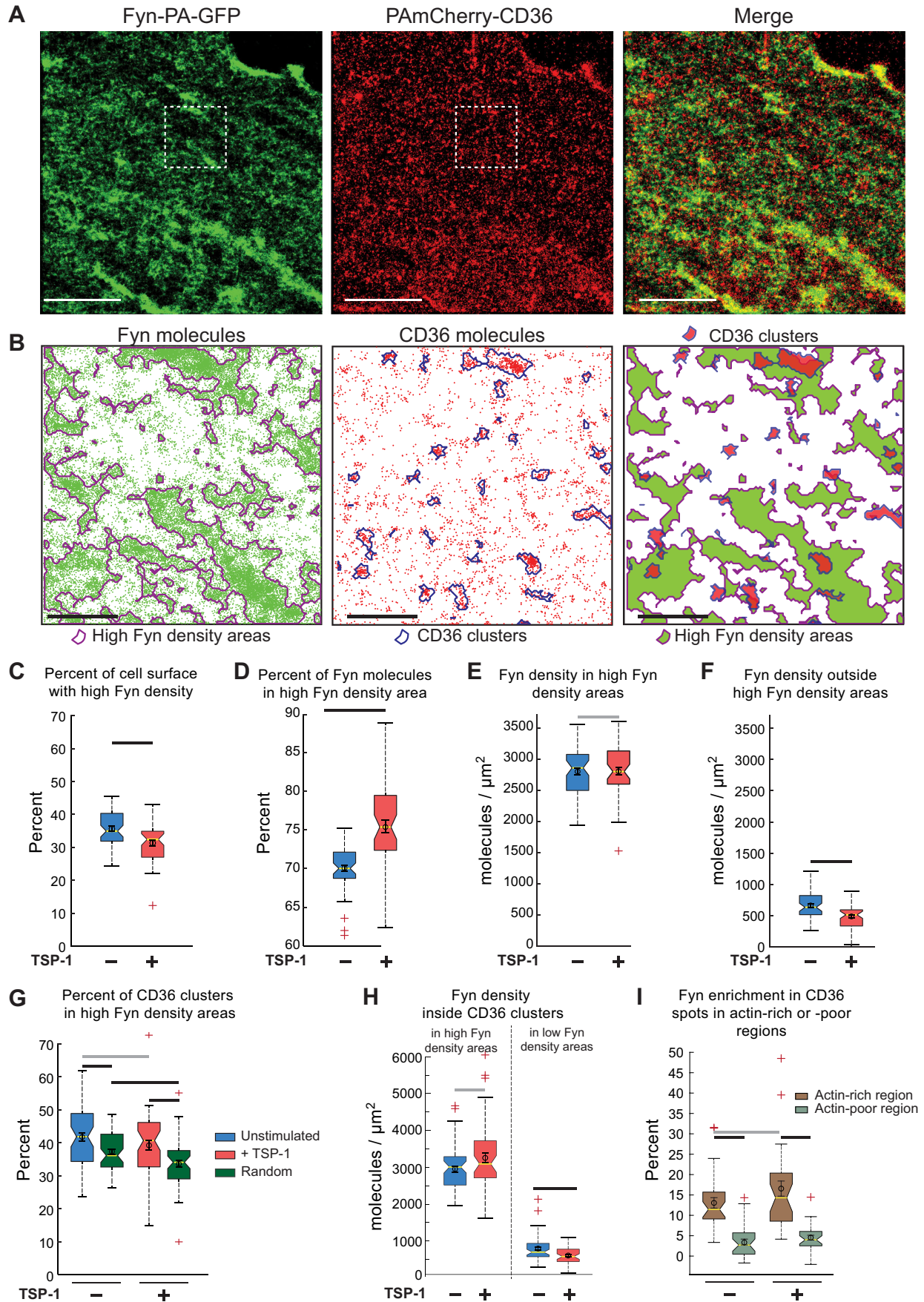
Fig. 3. See next page for legend.

Fig. 3. CD36 clusters in F-actin-rich regions are equally enriched with Fyn at all times. (A) Dual-color PALM of Fyn–PAGFP and PAmCherry–CD36. Scale bars: 5 µm. (B) Localized Fyn and CD36 molecules in the ROIs shown in A. High-Fyn-density areas and CD36 clusters, as determined by SPA, are outlined (left and middle) and overlaid (right). Scale bar: 1 µm. (C–H) Results of SPA in the absence or presence of TSP-1. The percentage of the cell surface that was covered with high-Fyn-density areas (C), percentage of Fyn molecules within high-Fyn-density areas (D), density of Fyn inside (E) and outside (F) high-Fyn-density areas, (G) percentage of CD36 clusters lying in high-Fyn-density areas from the experimental data (blue and red) or from randomized cluster positions (green), and Fyn density at CD36 clusters in high-Fyn (H, left) and low-Fyn (H, right) density areas. Data from 59 and 50 ROIs for untreated and treated cells, obtained in three independent experiments of 15 cells each. (I) Fyn enrichment at CD36 spots in actin-rich and -poor regions determined from TIRFM and enrichment analysis. Data from >30 fields of view acquired in three independent experiments, all imaged with identical settings. Boxplots and statistical tests in C–I are as described in Fig. 1E (for four comparisons in G and three comparisons in H; significance threshold=0.013 and 0.017, respectively, for each comparison).

-poor region, reflected by the actin enrichment value (Materials and Methods); and (iii) Fyn enrichment.

This analysis revealed that Fyn enrichment at CD36 clusters occurred primarily in F-actin-rich regions (Fig. 3I); 48–68% of detected CD36 clusters were in F-actin-rich regions. Consistent with the PALM data (Fig. 3G,H), Fyn enrichment at CD36 clusters in F-actin-rich regions was the same in the absence and presence of TSP-1. Using the unrelated transferrin receptor as a negative control (Fig. S3C,D) demonstrated that the observed Fyn enrichment at CD36 clusters in F-actin-rich regions was meaningful and not the result of a non-specific co-increase in signals owing to, for example, membrane ruffles. All in all, these analyses reveal that CD36 nanoclusters in F-actin-rich regions were enriched with Fyn at all times and that no additional Fyn recruitment occurred upon TSP-1 treatment.

CD36 cluster enhancement is sufficient for Fyn activation
The above results suggest that some change in CD36 and/or its nanoclusters upon TSP-1 binding led to Fyn activation because Fyn is enriched in CD36 clusters at all times. Our observation that anti-CD36 IgM (SMφ) activated Fyn to a similar level to that seen with TSP-1 (Fig. 1E) strongly implicated CD36 nanocluster enhancement in this process. This would be in contrast to, for example, a conformational change in CD36 upon TSP-1 binding or the action of other TSP-1 receptors (Adams and Lawler, 2011). To test for this, we performed PALM and SPA analysis of CD36 after stimulation with SMφ and after IgG treatment (FA6-152) as a negative control. Indeed, SMφ resulted in CD36 clusters that were similar in size and density to those produced by TSP-1, whereas FA6-152 produced clusters similar to those of unligated receptors (Fig. 4A,B). Plotting CD36 density inside clusters against cluster radius on an individual cluster basis showed that both TSP-1 and SMφ produced clusters that were larger and denser than those formed at rest (Fig. 4C).

To explicitly characterize the relationship between Fyn activation and the extent of CD36 clustering, we examined the localization of P-Y420 staining relative to CD36 clusters. Because Fyn enrichment at CD36 clusters was primarily along the actin cytoskeleton (Fig. 3I), here we used conventional TIRFM and enrichment analysis as above in order to simultaneously image CD36, P-Y420 and actin. HMEC-mApple–CD36 cells were fixed (after 10 min of ligand stimulation if present), permeabilized and stained with an Alexa-Fluor-488-conjugated antibody against P-Y420 and phalloidin–Alexa-Fluor-647 (Fig. S3B). We found that P-Y420

enrichment at CD36 clusters increased significantly upon TSP-1 or SMφ binding, further confirming the role of CD36 clusters in Fyn activation (Fig. 4D; Fig. S3E).

Plotting P-Y420 enrichment versus CD36 enrichment (a surrogate for the extent of clustering, combining size and density) on an individual cluster basis in F-actin-rich regions revealed a strong positive relationship between the extent of CD36 clustering and P-Y420 enrichment (Fig. 4E). This relationship was not observed in F-actin-poor regions, in which there was little P-Y420 enrichment at CD36 clusters (Fig. S3F). It was also not observed for total Fyn in F-actin-rich or F-actin-poor regions (Fig. 4F; Fig. S3).

The strong positive relationship between the extent of CD36 clustering and Fyn activation could be due to two reasons: CD36 cluster enhancement can lead to Fyn activation, or alternatively, Fyn activation – e.g. by CD36 multimerization through multivalent ligands – can lead to CD36 cluster enhancement. To distinguish between these two scenarios, we inhibited Fyn activation using the SFK inhibitor PP2 (10 µM for 15 min), which led to almost complete inhibition of Fyn activation by TSP-1 (Fig. 4G), and asked whether this prevented CD36 cluster enhancement (measured by PALM and SPA). This analysis revealed that the inhibition of Fyn activation had no effect on TSP-1-mediated enhancement of CD36 clustering, both in terms of cluster radius and CD36 density inside clusters (Fig. 4H,I). Overall, these data demonstrate that the enhancement of CD36 clustering through multivalent ligands is sufficient for Fyn activation at CD36 clusters.

Actin or cholesterol perturbation eliminates Fyn activation but not Fyn enrichment at CD36 clusters
The preferential enrichment and activation of Fyn at CD36 clusters in F-actin-rich regions suggested that actin could play a role in one or both of these processes. To test for this, we treated the cells with latrunculin B (LatB) to depolymerize F-actin, and measured Fyn activation and enrichment at CD36 clusters. To minimize cell disruption, we employed an acute treatment with a low concentration of LatB (200 nM for 15 min), which removed all visible actin stress fibers while retaining cell shape and adhesion to the coverslip (Fig. S4A). Actin disruption eliminated TSP-1-induced Fyn activation and phosphorylation of the downstream effectors p38MAPK (the antibody used here recognises MAPK11 to MAPK14) (Jiménez et al., 2000) and p130Cas (also known as BCAR1) (Fig. 5A–D). Activation of p130Cas downstream of CD36 in this pathway has not been reported previously but has been shown in other pathways (Davis et al., 2011; Stuart et al., 2007); yet actin disruption had no impact on Fyn enrichment at CD36 clusters in the absence or presence of TSP-1, as quantified by performing TIRFM and enrichment analysis (Fig. 5E).

We also tested whether membrane cholesterol plays a role in Fyn activation or enrichment at CD36 clusters. This was motivated by the fact that all four intracellular cysteine residues of CD36 are palmitoylated (Tao et al., 1996) and Fyn is myristoylated and doubly palmitoylated, which would increase their affinities for cholesterol-enriched nanodomains (Leventals et al., 2010; Lingwood and Simons, 2010). For this analysis, we measured Fyn activation and enrichment at CD36 clusters following cholesterol removal from the plasma membrane with methyl-β-cyclodextrin (MβCD). To minimize non-specific effects, we chose an acute and low concentration of MβCD (two 15-min periods of 2 mM MβCD), depleting cholesterol down to 50% (Fig. S4B,C) while preserving cell shape and adhesion to the coverslip (Fig. S4A). MβCD treatment eliminated TSP-1-induced Fyn activation and downstream signaling (Fig. 5A–D) upon TSP-1 treatment, but
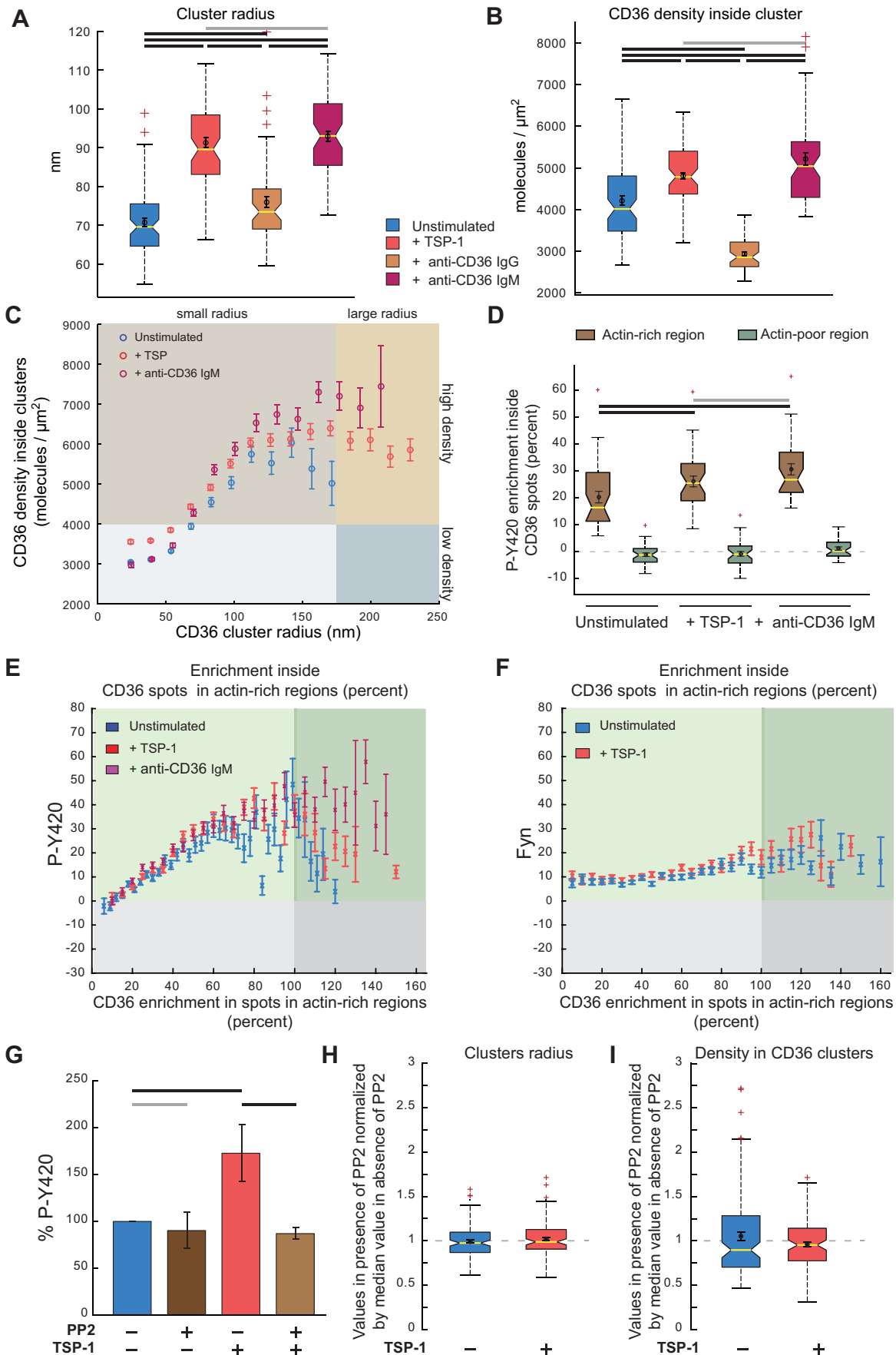
Fig. 4. See next page for legend.

Fig. 4. CD36 cluster enhancement is sufficient for Fyn activation.
(A,B) Cluster radius (A) and CD36 density within clusters (B) was determined by PALM and SPA of HMEC-PAmCherry–CD36 cells under specified conditions. Data from 59–63 ROIs per condition, imaged in three independent experiments, each containing ~10 different cells. Boxplots and statistical tests are as described in Fig. 1E (for six comparisons, significance threshold=0.0085 for each comparison). (C) Scatter plot of CD36 density inside clusters versus CD36 cluster radius on an individual cluster basis (i.e. not averaged over an ROI) for the ROIs shown in A. To clearly visualize trends, the clusters were grouped based on radius (x-axis), and the average density per group was calculated (y-axis). Circles and error bars indicate the mean and s.e.m. of each group, respectively. Colored quadrants are for visual guidance, and are set at the largest cluster radius and median density values for unstimulated cells. (D) P-Y420 enrichment at CD36 spots in actin-rich and -poor regions determined from TIRFM and enrichment analysis. Boxplots and statistical tests are as described in A (for three comparisons, significance threshold=0.017 for each comparison). Data from ~45 images acquired in three independent experiments with identical settings. (E,F) Scatter plot of P-Y420 (E) or Fyn (F) enrichment versus CD36 enrichment within mApple–CD36 spots on an individual spot basis in actin-rich regions. Analogous to the analysis in C, the CD36 spots were grouped based on CD36 enrichment value (x-axis), and the mean and s.e.m. of P-Y420 or Fyn enrichment per group was calculated. Data are from experiments described in D. Colored quadrants are for visual guidance and are set at 100% enrichment (i.e. doubling) for CD36 and 0% enrichment for P-Y420 or Fyn. (G) Fyn activation in the presence or absence of TSP-1±PP2 as assessed by immunoblotting. Quantification, error bars and statistical tests are as described in Fig. 1B. Data from three independent experiments. (H,I) Radius (H) and molecule density (I) of CD36 nanoclusters in the presence of PP2 relative to their values in its absence. The median relative value was not significantly different from 1 in all conditions, as indicated by the 95% confidence interval (i.e. notches). Data from ~60 ROIs obtained in three independent experiments of ten cells each.

again without any detectable effect on Fyn enrichment at CD36 clusters (Fig. 5E).

These data implicate actin and cholesterol in Fyn activation upon TSP-1–CD36 binding, but in a manner that is uncoupled from Fyn enrichment at CD36 clusters. They complemented our observations in unperturbed cells, where Fyn was activated by multivalent ligands (TSP-1 and SMφ) without any concomitant increase in Fyn enrichment at CD36 clusters. Because our data in unperturbed cells support the model that CD36 nanocluster enhancement by multivalent ligands is sufficient for Fyn activation, here, we hypothesized that Fyn is not activated in the presence of LatB or MβCD because they alter the nature of CD36 nanoclusters.

Actin or cholesterol perturbation reduces CD36 basal-state nanoclustering and TSP-1 binding

To test the hypothesis that the lack of Fyn activation by TSP-1 upon actin or cholesterol perturbation was due to the impairment of CD36 nanoclustering, we turned to PALM and SPA. The PALM image and localization quality measures were very similar with and without perturbations (Fig. S2B), allowing us to compare CD36 clustering properties in the absence and presence of LatB or MβCD. We found that, at basal state, these perturbations reduced the number and density of CD36 molecules within CD36 clusters, without altering the cluster radius (Fig. 6A–C). These changes are likely to reflect the decrease in CD36 density on the cell surface upon these acute perturbations (Fig. 6D).

Next we investigated whether this reduction in basal-state CD36 clustering reduced TSP-1 binding (Cambi et al., 2004; Cebecauer et al., 2010; Manzo et al., 2012). HMEC-mApple–CD36 cells that had been pre-treated with or without LatB or MβCD were fixed following a 10-min incubation with TSP-1, and bound TSP-1 was detected by immunofluorescent labeling and TIRFM (Fig. S4D). Cells expressing CD36 were masked, and CD36 expression and

TSP-1 binding levels were defined as the mean CD36 and TSP-1 intensities per cell, respectively. This analysis indicated that treatment with LatB or MβCD reduced TSP-1 binding by ~30% (Fig. S4E).

To uncouple the effects of reduced CD36 surface density versus reduced CD36 clustering on TSP-1 binding, we took advantage of cell–cell heterogeneity in CD36 expression levels within each condition to plot the TSP-1 binding level versus CD36 expression level on a per-cell basis (Fig. 6E). We quantified the relationship between TSP-1 and CD36 levels by fitting a straight line though the scatter of data points for each condition. If CD36 expression level was the only reason for reduced TSP-1 binding, all conditions would follow the same straight line. In contrast to this prediction, the different conditions followed distinct straight lines, with less TSP-1 binding per cell for the same CD36 expression level after drug-induced perturbation (Fig. 6E). These results indicate that CD36 basal-level nanoclustering promotes TSP-1 binding to HMVECs.

Actin or cholesterol perturbation hampers TSP-1-induced enhancement of CD36 nanoclustering

The ~30% reduction in TSP-1 binding upon LatB or MβCD treatment could not account for the complete elimination of signaling after these perturbations. Therefore, we investigated their effects on enhancement of CD36 nanoclustering by TSP-1. We found that, upon either perturbation, the size, density and number of molecules per cluster in the presence of TSP-1 remained below or close to the values for untreated cells at rest, never approaching the values for untreated cells that had been stimulated with TSP-1 (Fig. 6A–C). Plotting CD36 density inside clusters versus cluster radius revealed that neither perturbation allowed CD36 clusters to enter the larger size and higher density regime (Fig. 6F). This regime was occupied purely by clusters from unperturbed cells stimulated with TSP-1 or SMφ (Figs 6F and 4C). These analyses demonstrate that Fyn activation by TSP-1 required CD36 clusters that were both compact enough and large enough, an enhancement that depends on both the actin cytoskeleton and membrane cholesterol.

DISCUSSION

Using super-resolution imaging, we found that ~40% of CD36 molecules on the HMVEC surface are organized into basal-state nanoclusters that are enriched with Fyn (Figs 2, 3 and 7). Although unligated receptor clustering is thought to increase the efficiency of multivalent ligand binding (Cambi et al., 2004, 2006; Itano et al., 2012; Lillemeier et al., 2010; Mattila et al., 2013; Veatch et al., 2012), a notion supported by our results (Fig. 6), Fyn enrichment at CD36 clusters most likely plays a more crucial role for signaling. Specifically, this enrichment serves the purpose of keeping the receptor (CD36) and its signaling partner (Fyn) close to each other, ready to initiate signaling when exposed to ligand. Modeling efforts have previously suggested that clustering reduces the effective dissociation constant between molecules due to enhanced rebinding (Hsieh et al., 2010). We suspect that co-clustering or clustering and enrichment, as observed here, is a general mechanism to increase the signaling efficiency of receptors that signal through associated kinases, such as cytokine receptors and immunoreceptors (Garcia-Parajo et al., 2014; O'Shea and Murray, 2008).

If Fyn is enriched at CD36 clusters in the absence or presence of ligand, what prevents CD36–Fyn from signaling at all times, and what triggers Fyn activation upon TSP-1 binding? Our analyses indicate that CD36 nanocluster enhancement, increasing cluster size and density, as facilitated by binding to multivalent ligands such as TSP-1 and SMφ, is necessary and sufficient for Fyn activation and
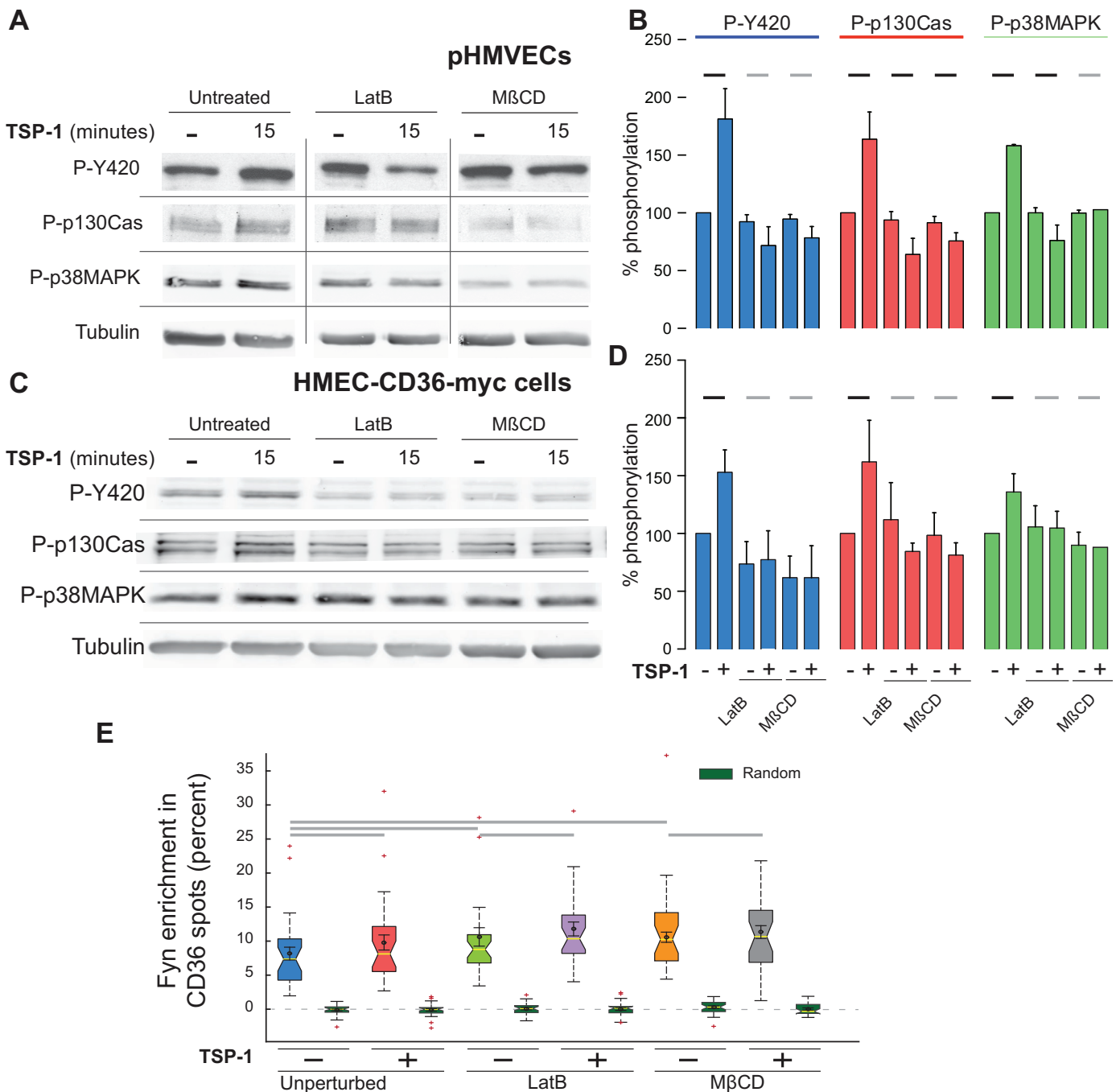
Fig. 5. Perturbation of actin or cholesterol inhibits Fyn activation but not Fyn enrichment at CD36 clusters. (A–D) Effect of LatB or MβCD on the phosphorylation levels of Fyn, p130Cas (P-p130Cas) and p38MAPK (P-p38MAPK) in pHMVECs (A,B) or HMEC-CD36–Myc cells (C,D), determined by immunoblotting. Tubulin was used as loading control. (A,C) Representative immunoblots. (B,D) Quantification of the percent phosphorylation normalized to the level in untreated control. Quantification, error bars and statistical tests are as described in Fig. 1B. Data are from three independent experiments. x-axis labels in D apply to B. (E) Fyn–mEmerald enrichment within mApple–CD36 spots under the indicated conditions compared to randomized control (green boxes). Boxplots and statistical tests are as described in Fig. 1E (for five comparisons, significance threshold=0.01 for each comparison).

downstream signaling. Necessity is demonstrated by the abrogation of TSP-1-induced Fyn and downstream effector activation when proper CD36 cluster enhancement is hindered upon F-actin or cholesterol perturbation (Figs 5 and 6). Sufficiency is demonstrated by the ability of SMφ to activate Fyn by merely enhancing CD36 clustering, similar to the action of TSP-1 (Fig. 4). The positive relationship, at the level of individual clusters, between the extent of CD36 clustering and Fyn activation (Fig. 4) is consistent with the necessity and sufficiency of cluster enhancement to activate Fyn.

Our data suggest that there might also be low levels of 'tonic' Fyn activation in the absence of ligand (Treanor et al., 2010). This is demonstrated by the decreased levels of P-Y420 at rest following unligated cluster disruption with LatB or MβCD, or following RNAi-mediated Fyn depletion (Figs 1 and 5). Tonic signaling might be due to the inherent heterogeneity of resting CD36 clusters, such that a (very) small subset of clusters can at times reach the right size and density to activate Fyn. The need for both larger and denser clusters might, however, minimize tonic signaling.
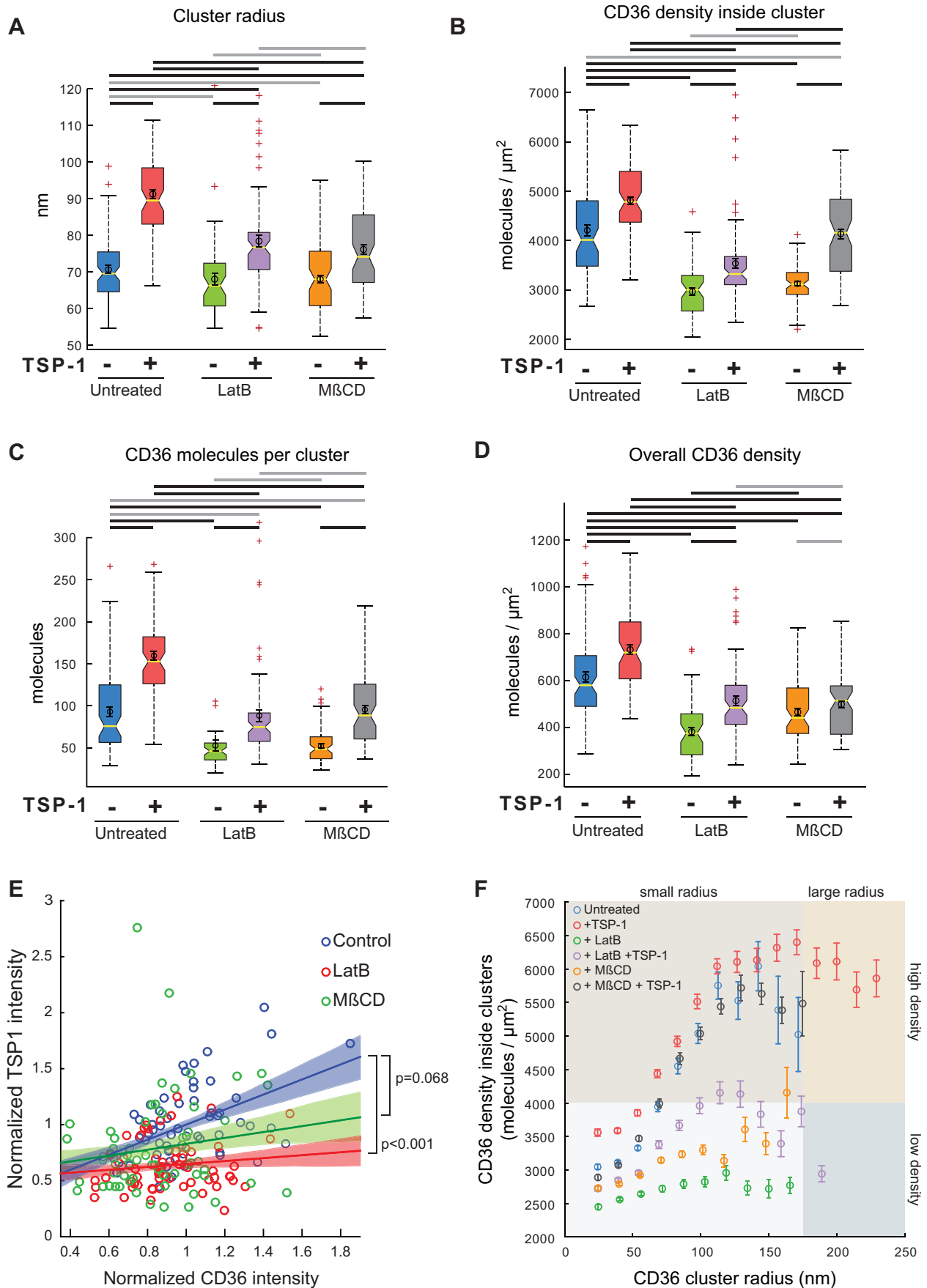
Fig. 6. See next page for legend.

Fig. 6. Perturbation of actin or cholesterol reduces the basal-state and ligated nanoclustering of CD36. (A–D) Cluster radius (A), density of CD36 molecules in clusters (B), number of molecules per cluster (C) and overall CD36 density (D) as derived from PALM and SPA of HMEC-PAmCherry–CD36 cells under the indicated conditions. Data are from 51–81 ROIs per condition, each imaged in three independent experiments, each containing 7–10 different cells. Boxplots and statistical tests are as described in Fig. 1E (for 11 comparisons, significance threshold=0.0047 for each comparison). (E) Scatter plot of TSP-1 intensity versus CD36 intensity per cell, from TIRFM images of HMEC-mApple–CD36 cells immunostained for bound TSP-1. Measurements were normalized to their mean values under the unperturbed condition. Heavy lines represent the least squares fit of a straight line (slope and *y*-intercept determined by fit) through the corresponding (similar color) data points. Shading around each line shows ±1 s.d. of the slope and *y*-intercept, taking their covariance into account. *P*-values comparing the fitted lines (slope and intercept together, using a full variance–covariance matrix) were obtained using a chi-squared distribution. (F) Scatter plot of CD36 density inside clusters versus CD36 cluster radius on an individual cluster basis, as in Fig. 4C, from the ROIs described in A.

The molecular mechanisms that link CD36 cluster growth and compaction to Fyn activation are currently unknown and warrant further investigation. One possibility is that CD36 cluster growth increases the dwell time of Fyn inside CD36 clusters, thus facilitating

its activation. Another possibility is that CD36 cluster compaction facilitates inter-molecular interactions that lead to Fyn activation. Our study provides leads to guide these future investigations.

In conclusion, we propose a new model of CD36–Fyn organization and signaling that is likely to be applicable to many other signaling pathways (Fig. 7). Instead of a model of purely diffusing molecules, in which receptors must randomly encounter both ligand and downstream effector, our data demonstrate that CD36 is organized into basal-state nanoclusters. In addition to facilitating ligand binding, we discovered that basal-state nanoclusters are enriched with the downstream effector Fyn (or conversely, they form in areas rich in Fyn molecules), effectively forming a 'receptor–transducer duo'. This arrangement is crucial for signaling; our data demonstrate that Fyn activation upon TSP-1 binding is not due to its de novo recruitment into CD36 nanoclusters but instead due to ligand-induced enhancement of CD36 nanoclusters. Nanocluster enhancement does not depend only on ligand but also on membrane cholesterol and the actin cytoskeleton – i.e. the membrane ultrastructure. Our study emphasizes the need for further exploration of the role of the membrane ultrastructure in the regulation of receptor nanoclustering and signaling.
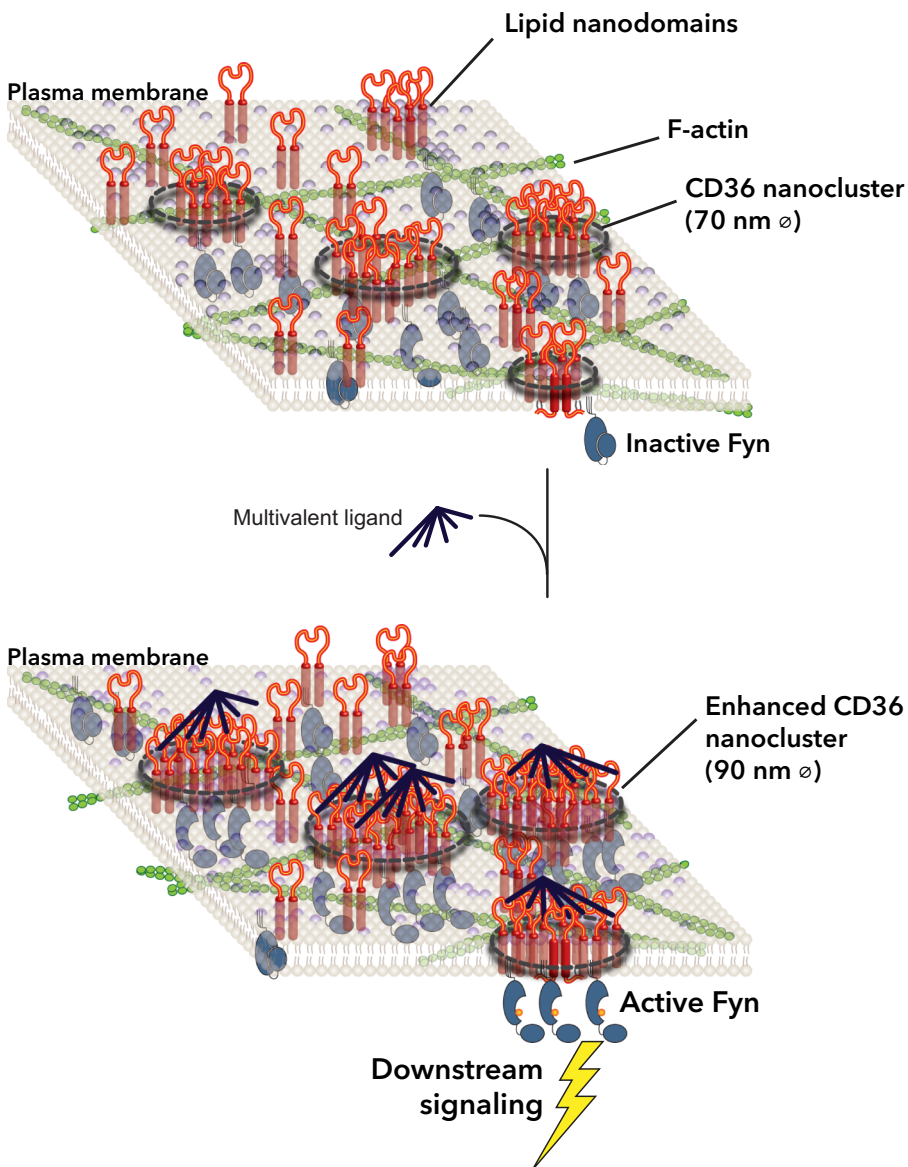

Fig. 7. Schematic representation of CD36 nanoclustering, Fyn enrichment and signaling. Top panel: at steady state, CD36 molecules are organized into nanoclusters (radius ∼70 nm, black circles) that are enriched with the effector kinase Fyn. Bottom panel: multivalent ligands such as TSP-1 or SMφ enhance clustering, resulting in Fyn activation. Cluster enhancement is supported by the plasma membrane ultrastructure – e.g. by lipid nanodomains and cortical F-actin.

MATERIALS AND METHODS

Cell culture
HMEC-1 cells (CDC) were cultured as previously described (Ades et al., 1992). Primary HMVECs (Lonza) were cultured following manufacturer instructions. Stable expression of CD36 constructs in HMEC-1 cells was achieved using viral transfection (described below). Transient transfections were performed using FugeneHD (Promega) following the manufacturer's instructions.

Plasmids
Human CD36 cDNA was obtained from Origene (OriGene Technologies). The coding sequence was amplified with primers containing a BspEI site (5′) and an EcoRI site (3′). The purified fragment was digested with these enzymes and ligated at the 5′ end of mApple and PAmCherry. The same strategy was used to generate Fyn–mEmerald and Fyn–PAGFP vectors. Human Fyn cDNA was obtained from the Harvard University plasmid repository PlasmidID. Each CD36 construct (CD36–Myc, mApple–CD36 and PAmCherry–CD36) was subcloned into retroviral vector pFB-Neo using AgeI and NotI restriction sites (Stratagene). These were then co-transfected with pVPack-VSV-G and pVPack-GP vectors into HEK 293T cells for virus production. Virus was used to transduce HMEC-1 cells for 24 h when 1 mg/ml G418 (Sigma-Aldrich) was added to the culture medium. Selection was performed for 14 days to generate stable cell lines. Expression was confirmed by immunoblotting and immunofluorescence labeling.

Plasmids for CD36, Fyn and transferrin receptor tagged with fluorescent proteins are available from Addgene (plasmid numbers 54100, 54874, 54278, respectively).

Immunoblotting
Fyn, p38MAPK and p130Cas phosphorylation was analyzed with anti-P-Y420 (#44660G, Invitrogen; 1:500), anti-phosphorylated-p38MAPK (#9211, Cell Signaling; 1:1000) and anti-phosphorylated-p130Cas (#4011, Cell Signaling; 1:1000) antibodies, respectively. Anti-Fyn (#4023, Cell Signaling; 1:1000), anti-Src (#2123, Cell Signaling; 1:1000) and anti-tubulin (T5168, Sigma-Aldrich; 1:10,000) antibodies were used to probe for total Fyn, Src and tubulin, respectively. Cells were grown on 6-well-plates coated with 1 µg/cm^2 fibronectin (BD Biosciences). Serum-starvation was performed for 3 h using MBCD-131 medium, after which 10 nM of TSP-1 (Protein Sciences) was added for the indicated time. Cells were lysed using phosphorylation lysis buffer (20 mM MOPS, 1% Triton X-100, 1 mM sodium orthovanadate, 2 mM EGTA, 5 mM EDTA, pH 7.0) supplemented with PhosSTOP (Roche Applied Science) and protease inhibitor (Sigma-Aldrich). The lysates were resolved on SDS-PAGE gels, transferred to nitrocellulose membranes and immunoblotted with the antibodies described above. The membranes were then incubated with the appropriate IRDye-coupled secondary antibodies (LI-COR Biosciences). The Odyssey Infrared Imaging System scanner (LI-COR Biosciences) was used to scan for the immunoblotted proteins in the 700-nm and 800-nm channels. Quantification of the band intensities was performed using ImageJ, and the relative amount of phosphorylation was normalized either to total protein amount (for Fyn) or to loading control (tubulin; for p38MAPK and p130CAS).

Drug treatment
Cells were incubated with 200 nM LatB (Sigma-Aldrich), 2 mM MβCD (Sigma-Aldrich) or 10 µM PP2 (Sigma-Aldrich) in MBCD-131 medium for 15 min. Drug treatment was maintained during TSP-1 stimulation by adding the drugs with TSP-1 when used.

Cholesterol assay
A cholesterol assay kit (Abcam) was used to measure the effects of MβCD or LatB treatment on cholesterol levels. Cells were treated with 200 nM LatB or 2 mM MβCD for 15 min at 37°C and stained with Filipin-III following the manufacturer's instructions. Cells were imaged using identical parameters on a wide-field Olympus IX81 microscope using brightfield and Cy5 configurations. Mean Filipin-III fluorescence intensity was measured for each cell and normalized to the average fluorescence intensity of control cells.

siRNA knockdown
HMVECs were grown to about 80% confluence. On-Target SMARTpool siRNAs against CD36, Fyn or Src, or a nonspecific siRNA (Thermo Scientific), were prepared at a concentration of 10 µM in nuclease-free water. 90 pmol of the siRNA was mixed with RNAiMAX reagent (Life Technologies) at a 1:1 volume ratio in Opti-MEM medium (Gibco, Life Technologies). The complexes were incubated for 10 min at room temperature. The siRNA–reagent complex was added to cells and incubated for 48 h before the intended experiment was performed.

Immunofluorescence
Cells were grown on Lab-Tek chambers (Fisher Scientific) that had been coated with 1 µg/cm^2 fibronectin (BD Biosciences). Serum-starvation was performed for 3 h using the MBCD-131 medium before stimulation with or without 10 nM TSP-1, 10 µg/ml FA6-152 (Santa Cruz Biotechnology) or 10 µg/ml SMφ (Santa Cruz Biotechnology) for the intended timepoints. This was followed by fixation with 3% paraformaldehyde (PFA) (Canemco) and 0.1% glutaraldehyde (Canemco) in PBS for 10 min at 4°C. Quenching was performed with 0.1% sodium borohydride (Sigma-Aldrich) in PBS for 7 min. For CD36 surface staining, cells were blocked with blocking buffer (3% BSA in PBS) for 30 min and then incubated with 1:1000 monoclonal mouse anti CD36 IgG (clone FA6-152) in blocking buffer for 30 min, followed by incubation with anti-mouse antibody conjugated to Alexa-Fluor-488, Cy3 or Alexa-Fluor-647 (Jackson ImmunoResearch) diluted in blocking buffer. For intracellular staining, 0.1% Triton X-100 in PBS was used for cell permeabilization. Active Fyn was stained with anti-P-Y420 conjugated to Alexa-Fluor-488 (Invitrogen) in blocking buffer after intracellular blocking. Actin was labeled with phalloidin Alexa-Fluor-488, Alexa-Fluor-555 or Alexa-Fluor-647 (Invitrogen) depending on the experiment. DAPI (Sigma-Aldrich) was used to stain cell nuclei.

Flow cytometry
Comparative assessment of cell surface CD36 expression in pHMVECs and HMEC-1-derived stable cell lines was determined by performing flow cytometry. Cells grown in a 10-cm dish were resuspended using 1 ml of Accutase (Gibco, Life Technologies) for 5 min at 37°C and harvested by performing centrifugation (100 g for 4 min). Following fixation with 4% PFA for 10 min, cells were immunostained by successive centrifugations and resuspensions and incubations (30 min) in the following buffers: (1) blocking buffer (3% BSA in PBS); (2) blocking buffer containing 1:1000 monoclonal mouse anti-CD36 IgG (clone FA6-152); (3) blocking buffer containing 1:1000 anti-mouse-IgG antibody conjugated to Alexa-Fluor-647. Each antibody incubation was followed by two washes with PBS. Cell surface stained CD36 was measured using an Accuri C6 flow cytometer (BD Accuri). Non-stained control cells were used to gate CD36-expressing cells. The fraction of cells expressing CD36 was determined by the ratio of cells found within the gate compared to the total cell numbers. The median fluorescence intensity of the resultant fluorescence histogram was used to measure CD36 expression levels, and the relative expression levels were normalized to the levels in pHMVECs.

TSP-1 labeling
TSP-1 was labeled using fluorescent dyes (Cy3b or Atto647N) N-hydroxysuccinimide (NHS) esters (GE healthcare and Sigma-Aldrich). 0.02 mg of the dye was dissolved in 10 µl anhydrous DMSO. 10 µg of TSP-1 was added to 20 µl of 0.5 M NaHCO$_3$ (pH 8.5) with 5 µl of the dye solution. The reaction was incubated for 1 h in the dark, rocking gently at room temperature. After the reaction, labeled TSP-1 was separated and recovered in the void volume of a NAP-5 column (GE Healthcare). TSP-1 conjugation was confirmed using a NanoDrop spectrophotometer (Thermo Scientific).

Pulse–chase endocytosis–exocytosis assay
HMEC-CD36–Myc cells were grown on Lab-Tek chambers that had been coated with 1 µg/cm^2 fibronectin. To measure CD36 endocytosis, anti-CD36 Fab fragments were generated from monoclonal anti-CD36 IgG (clone 131.2, gift from Dr Narendra Tandon, Otsuka America

4186

Pharmaceutical, Inc., Rockville, MD) using Pierce™ Fab Preparation Kit (Thermo Fisher). The Fabs were labeled with fluorescent Cy3b NHS esters, as described for TSP-1 above. The anti-CD36–Cy3b Fabs were bound to CD36–Myc-expressing cells on ice, followed by a 10-min incubation at 37° C with or without TSP-1. Surface-bound antibodies were acid-washed on ice (acid wash solution: 500 mM glacial acetic acid, 150 mM NaCl, pH 2.5) for 2 min followed by a 2-min recovery with MBCD-131 medium and an additional 2-min incubation in the acid wash solution. Cells were fixed and stained with Alexa-Flour-488 anti-mouse secondary antibody following the immunofluorescence protocol above. The extent of CD36 endocytosis was determined by epi-fluorescence microscopy imaging by measuring the amount of internalized anti-CD36–Cy3b Fab.

To measure CD36 exocytosis, all surface CD36 was bound with mouse anti-CD36 Fabs in MBCB-131 medium on ice using a saturating antibody concentration (1:250). Unbound antibodies were washed off with cold medium, followed by a 10-min incubation at 37°C with or without TSP-1. Cells were fixed using the immunofluorescence protocol. Pre-bound CD36 Fabs were detected using Alexa-Flour-488 anti-mouse antibody. The unbound CD36 fraction (exocytosed fraction) was then labeled with monoclonal mouse anti-CD36–Cy3b Fabs. The extent of CD36 exocytosis was determined using TIRFM by measuring the amount of anti-CD36–Cy3b Fab that had bound.

Confocal microscopy
Confocal imaging was performed on a Quorum Technologies WaveFx spinning disk microscope with a 60×1.42 NA oil objective, using an electron multiplying charge coupled device (EM-CCD) camera (Hamamatsu) and Volocity software (PerkinElmer) set up on an Olympus IX-81 inverted stand.

TIRFM and PALM
TIRFM was performed on an Olympus IX-81 base installed by Quorum Technologies. Acquisition was done using 100× (1.45 NA) oil objective, with an EM-CCD camera (ImageEM91013, Hamamatsu) using Volocity software (PerkinElmer).

For PALM, cells were fixed on ice with 3% PFA and 0.2% glutaraldehyde. The coverslips were incubated before cell plating with multichannel tetraspec beads (Invitrogen) as fiducial markers. Image acquisition was performed with Metamorph software (Molecular Devices). A low-power (20 µW) 405-nm laser (Spectral Applied Research) was used to photo-activate PAmCherry–CD36 molecules, of which the fluorescent signal was acquired at 605 nm after excitation with 1 mW of 561-nm laser power (Spectral Applied Research) at 10 frames per second (fps) until all molecules had been photobleached (typically 5000 frames). For dual-color PALM, Fyn–PAGFP fluorescence was acquired first, using 1 mW of a 491-nm laser (Spectral Applied Research) to simultaneously photoactivate and image it at 10 fps until all molecules had been photobleached (Sengupta et al., 2011). PAmCherry–CD36 was then imaged as described above.

PALM image analysis
PALM images were analyzed using Gaussian-mixture-model fitting (Jaqaman et al., 2008; Thomann et al., 2002), which yielded molecular positions in each image of the PALM sequence. The localization precision of each molecule was 18 nm on average (Fig. S2B), with an average of 460 photons per localization. Image and localization quality (background level, noise level, localization precision, molecule amplitude and number of repeated appearances by each molecule) were very similar between all studied conditions (Fig. S2B). Localizations with precision above 50 nm (~0.0004% of all the localizations) were eliminated from further analysis. Lateral drift was corrected for using fiducial marker localization and tracking.

To avoid molecule over-counting due to repeated emission by the same molecule, the localized molecules were then tracked using a previously developed particle-tracking algorithm (u-track; Jaqaman et al., 2008, accessible at http://www.utsouthwestern.edu/labs/jaqaman/software/), using a search radius of 1 pixel and a gap closing time window of three frames. This accounted for repeated emission and potential short-term

blinking, but not potential long-term blinking, which was, however, expected to be minimal for PAmCherry and PAGFP (Durisic et al., 2014). This analysis was able to eliminate localization multi-appearances as evident from the pair-correlation function (Puchner et al., 2013) (Fig. S2A). For each molecule that appeared in more than one frame (20–30% of all molecules; Fig. S2B), its final position was taken as the weighted average position of its multiple appearances (weight determined by individual localization precisions), equivalent to photon pooling. With this, the localization precision of a molecule that appeared for N frames was improved by a factor of $\sim \sqrt{N}$.

SPA
This analysis was done as described previously by Owen et al. (Owen et al., 2010; Williamson et al., 2011), using a 50-nm radius to calculate the second order neighborhood value L_i for each coordinate i and generate cluster spatial maps. 3–4 non-overlapping 4×4 µm^2 regions of interest (ROIs) were cropped from each imaged cell for this analysis.

To obtain CD36 cluster properties, we developed on top of the Owen et al. analysis a robust and unbiased thresholding approach to segment the local density spatial maps and identify receptor clusters. Specifically, we randomized an equal number of receptor positions within each ROI, assigned each randomized receptor a local density using the same 50-nm radius as the real data, then took the maximum local density $L_{max-rand}$ for the randomized receptors as the threshold. Any coordinate i in the real receptor dataset with an $L_i>L_{max-rand}$ was considered to be in a cluster. Based on this threshold, binary spatial maps were generated to extract CD36 cluster features (Fig. 2E).

The accuracy of this analysis in extracting cluster properties was assessed using simulated data. Coordinates with known cluster properties and varying numbers of clusters per area, numbers of molecules per cluster, density inside versus density outside clusters, and cluster radius were generated. The ranges of cluster properties were based on CD36 data (with and without ligands and drug perturbations). The calculated cluster properties were compared to the simulation ground truth properties using 150 simulations. Dividing the calculated property values by the ground truth values revealed that our thresholding scheme recovers cluster properties with an accuracy >95% (Fig. S2F).

To identify cell surface areas with higher-than-average Fyn density, we followed the same procedure as above, except that the threshold was taken as the median local density $L_{med-rand}$ for randomized Fyn coordinates. Based on this threshold, binary spatial maps were generated to classify cell surface areas as high Fyn or low Fyn density.

Intensity enrichment analysis
For the enrichment analysis of species X (X=Fyn, P-Y420, actin, transferrin receptor or CD36) at CD36 spots (representing nanoclusters) from multi-color immunofluorescence TIRFM images, the centers of CD36 spots were determined using Gaussian-mixture-model fitting (Jaqaman et al., 2008), and each CD36 spot was taken as a circular area of radius 3 pixels around the center position, reflecting the point spread function (PSF) of the microscope. The intensity in all channels was corrected for non-uniform background as follows: (i) a background image was estimated by filtering the image with a wide Gaussian (standard deviation 10 pixels), (ii) this background image was subtracted from the original image, and (iii) the average raw image intensity value was added back to avoid dividing by zero in the ratio calculation. Only areas within the cell mask (see next section) were used for analysis. The mean F-actin enrichment value after CD36 spot randomization within the cell mask was taken as the divider to separate CD36 spots in F-actin-rich regions (F-actin ratio>randomization mean) and in F-actin-poor regions. The analysis was written in MATLAB (MathWorks) and is available at http://www.utsouthwestern.edu/labs/jaqaman/software/.

Cell mask segmentation
Cell mask segmentation was based on the channel with most continuous (i.e. spatially smooth, not punctate) signal. Because multiple levels of intensity were often present due to heterogeneity in molecular distribution, a generalized Otsu

approach was used to determine n thresholds for an image, together with a metric that measures the confidence of using these n thresholds. For any given image, the number of thresholds n with the highest confidence metric was selected. Among these n thresholds, the threshold value that had the greatest distance between it and the preceding threshold value was taken as the cell mask threshold, motivated by the fact that the largest intensity difference within an image is the difference between inside and outside the cell.

Graph and statistical analysis

Bar graphs showing quantification of immunoblot data were generated using GraphPad Prism (Graphpad Software). All other graphing and statistical analyses were performed in MATLAB (MathWorks). Statistical tests to compare different conditions are described in the legend of Fig. 1.

Competing interests
The authors declare no competing or financial interests.

Author contributions
K.J. and N.T. conceived and directed study. J.M.G. performed experiments and SPA. A.R.V. performed enrichment analysis. M.A.B. and M.W.D. generated fluorescent proteins fusions.

Supplementary information
Supplementary information available online at
http://jcs.biologists.org/lookup/doi/10.1242/jcs.188946.supplemental

References
Adams, J. C. and Lawler, J. (2011). The thrombospondins. *Cold Spring Harb. Perspect. Biol.* **3**, a009712.

Ades, E. W., Candal, F. J., Swerlick, R. A., George, V. G., Summers, S., Bosse, D. C. and Lawley, T. J. (1992). HMEC-1: establishment of an immortalized human microvascular endothelial cell line. *J. Invest. Dermatol.* **99**, 683-690.

Betzig, E., Patterson, G. H., Sougrat, R., Lindwasser, O. W., Olenych, S., Bonifacino, J. S., Davidson, M. W., Lippincott-Schwartz, J. and Hess, H. F. (2006). Imaging intracellular fluorescent proteins at nanometer resolution. *Science* **313**, 1642-1645.

Cambi, A., de Lange, F., van Maarseveen, N. M., Nijhuis, M., Joosten, B., van Dijk, E. M. H. P., de Bakker, B. I., Fransen, J. A. M., Bovee-Geurts, P. H. M., van Leeuwen, F. N. et al. (2004). Microdomains of the C-type lectin DC-SIGN are portals for virus entry into dendritic cells. *J. Cell Biol.* **164**, 145-155.

Cambi, A., Joosten, B., Koopman, M., de Lange, F., Beeren, I., Torensma, R., Fransen, J. A., Garcia-Parajó, M., van Leeuwen, F. N. and Figdor, C. G. (2006). Organization of the integrin LFA-1 in nanoclusters regulates its activity. *Mol. Biol. Cell* **17**, 4270-4281.

Cebecauer, M., Spitaler, M., Serge, A. and Magee, A. I. (2010). Signalling complexes and clusters: Functional advantages and methodological hurdles. *J. Cell Sci.* **123**, 309-320.

Davis, S. P., Amrein, M., Gillrie, M. R., Lee, K., Muruve, D. A. and Ho, M. (2011). Plasmodium falciparum-induced CD36 clustering rapidly strengthens cytoadherence via p130CAS-mediated actin cytoskeletal rearrangement. *FASEB J.* **26**, 1119-1130.

Dawson, D. W., Pearce, S. F. A., Zhong, R., Silverstein, R. L., Frazier, W. A. and Bouck, N. P. (1997). CD36 mediates the in vitro inhibitory effects of thrombospondin-1 on endothelial cells. *J. Cell Biol.* **138**, 707-717.

Dempsey, G. T., Vaughan, J. C., Chen, K. H., Bates, M. and Zhuang, X. (2011). Evaluation of fluorophores for optimal performance in localization-based super-resolution imaging. *Nat. Methods* **8**, 1027-1036.

Durisic, N., Laparra-Cuervo, L., Sandoval-Álvarez, A., Borbely, J. S. and Lakadamyali, M. (2014). Single-molecule evaluation of fluorescent protein photoactivation efficiency using an in vivo nanotemplate. *Nat. Methods* **11**, 156-162.

Fish, K. N. (2009). Total internal reflection fluorescence (TIRF) microscopy. *Curr. Protoc. Cytom.* Chapter 12, Unit12.18.

Garcia-Parajo, M. F., Cambi, A., Torreno-Pina, J. A., Thompson, N. and Jacobson, K. (2014). Nanoclustering as a dominant feature of plasma membrane organization. *J. Cell Sci.* **127**, 4995-5005.

Hoosdally, S. J., Andress, E. J., Wooding, C., Martin, C. A. and Linton, K. J. (2009). The human scavenger receptor CD36: Glycosylation status and its role in trafficking and function. *J. Biol. Chem.* **284**, 16677-16288.

Hsieh, M.-y., Yang, S., Raymond-Stinz, M. A., Edwards, J. S. and Wilson, B. S. (2010). Spatio-temporal modeling of signaling protein recruitment to EGFR. *BMC Syst. Biol.* **4**, 57.

Itano, M. S., Steinhauer, C., Schmied, J. J., Forthmann, C., Liu, P., Neumann, A. K., Thompson, N. L., Tinnefeld, P. and Jacobson, K. (2012). Super-resolution imaging of C-type lectin and influenza hemagglutinin nanodomains on plasma membranes using blink microscopy. *Biophys. J.* **102**, 1534-1542.

Jaqaman, K. and Grinstein, S. (2012). Regulation from within: the cytoskeleton in transmembrane signaling. *Trends Cell Biol.* **22**, 515-526.

Jaqaman, K., Loerke, D., Mettlen, M., Kuwata, H., Grinstein, S., Schmid, S. L. and Danuser, G. (2008). Robust single-particle tracking in live-cell time-lapse sequences. *Nat. Methods* **5**, 695-702.

Jaqaman, K., Kuwata, H., Touret, N., Collins, R., Trimble, W. S., Danuser, G. and Grinstein, S. (2011). Cytoskeletal control of CD36 diffusion promotes its receptor and signaling function. *Cell* **146**, 593-606.

Jiménez, B., Volpert, O. V., Crawford, S. E., Febbraio, M., Silverstein, R. L. and Bouck, N. (2000). Signals leading to apoptosis-dependent inhibition of neovascularization by thrombospondin-1. *Nat. Med.* **6**, 41-48.

Klenotic, P. A., Page, R. C., Li, W., Amick, J., Misra, S. and Silverstein, R. L. (2013). Molecular basis of antiangiogenic thrombospondin-1 type 1 repeat domain interactions with CD36. *Arterioscler. Thromb. Vasc. Biol.* **33**, 1655-1662.

Leventa, I., Lingwood, D., Grzybek, M., Coskun, U. and Simons, K. (2010). Palmitoylation regulates raft affinity for the majority of integral raft proteins. *Proc. Natl. Acad. Sci. USA* **107**, 22050-22054.

Lillemeier, B. F., Mörtelmaier, M. A., Forstner, M. B., Huppa, J. B., Groves, J. T. and Davis, M. M. (2010). TCR and lat are expressed on separate protein islands on T cell membranes and concatenate during activation. *Nat. Immunol.* **11**, 90-96.

Lingwood, D. and Simons, K. (2010). Lipid rafts as a membrane-organizing principle. *Science* **327**, 46-50.

Manzo, C., Torreno-Pina, J. A., Joosten, B., Reinieren-Beeren, I., Gualda, E. J., Loza-Alvarez, P., Figdor, C. G., Garcia-Parajo, M. F. and Cambi, A. (2012). The neck region of the C-type lectin DC-SIGN regulates its surface spatiotemporal organization and virus-binding capacity on antigen-presenting cells. *J. Biol. Chem.* **287**, 38946-38955.

Mattila, P. K., Feest, C., Depoil, D., Treanor, B., Montaner, B., Otipoby, K. L., Carter, R., Justement, L. B., Bruckbauer, A. and Batista, F. D. (2013). The actin and tetraspanin networks organize receptor nanoclusters to regulate B cell receptor-mediated signaling. *Immunity* **38**, 461-474.

Mattila, P. K., Batista, F. D. and Treanor, B. (2016). Dynamics of the actin cytoskeleton mediates receptor cross talk: an emerging concept in tuning receptor signaling. *J. Cell Biol.* **212**, 267-280.

Morone, N., Fujiwara, T., Murase, K., Kasai, R. S., Ike, H., Yuasa, S., Usukura, J. and Kusumi, A. (2006). Three-dimensional reconstruction of the membrane skeleton at the plasma membrane interface by electron tomography. *J. Cell Biol.* **174**, 851-862.

O'Shea, J. J. and Murray, P. J. (2008). Cytokine signaling modules in inflammatory responses. *Immunity* **28**, 477-487.

Owen, D. M., Rentero, C., Rossy, J., Magenau, A., Williamson, D., Rodriguez, M. and Gaus, K. (2010). PALM imaging and cluster analysis of protein heterogeneity at the cell surface. *J. Biophoton.* **3**, 446-454.

Primo, L., Ferrandi, C., Roca, C., Marchiò, S., di Blasio, L., Alessio, M. and Bussolino, F. (2005). Identification of CD36 molecular features required for its in vitro angiostatic activity. *FASEB J.* **19**, 1713-1715.

Puchner, E. M., Walter, J. M., Kasper, R., Huang, B. and Lim, W. A. (2013). Counting molecules in single organelles with superresolution microscopy allows tracking of the endosome maturation trajectory. *Proc. Natl. Acad. Sci. USA* **110**, 16015-16020.

Saito, Y. D., Jensen, A. R., Salgia, R. and Posadas, E. M. (2010). Fyn: a novel molecular target in cancer. *Cancer* **116**, 1629-1637.

Sengupta, P., Jovanovic-Talisman, T., Skoko, D., Renz, M., Veatch, S. L. and Lippincott-Schwartz, J. (2011). Probing protein heterogeneity in the plasma membrane using PALM and pair correlation analysis. *Nat. Methods* **8**, 969-975.

Silverstein, R. L. and Febbraio, M. (2009). CD36, a scavenger receptor involved in immunity, metabolism, angiogenesis, and behavior. *Sci. Signal.* **2**, re3.

Simons, K. and Gerl, M. J. (2010). Revitalizing membrane rafts: new tools and insights. *Nat. Rev. Mol. Cell Biol.* **11**, 688-699.

Soares, H., Henriques, R., Sachse, M., Ventimiglia, L., Alonso, M. A., Zimmer, C., Thoulouze, M.-I. and Alcover, A. (2013). Regulated vesicle fusion generates signaling nanoterritories that control T cell activation at the immunological synapse. *J. Exp. Med.* **210**, 2415-2433.

Stuart, L. M., Bell, S. A., Stewart, C. R., Silver, J. M., Richard, J., Goss, J. L., Tseng, A. A., Zhang, A., El Khoury, J. B. and Moore, K. J. (2007). CD36 signals to the actin cytoskeleton and regulates microglial migration via a p130Cas complex. *J. Biol. Chem.* **282**, 27392-27401.

Tang, Q. and Edidin, M. (2001). Vesicle trafficking and cell surface membrane patchiness. *Biophys. J.* **81**, 196-203.

Tao, N., Wagner, S. J. and Lublin, D. M. (1996). CD36 is palmitoylated on both N- and C-terminal cytoplasmic tails. *J. Biol. Chem.* **271**, 22315-22320.

Thomann, D., Rines, D. R., Sorger, P. K. and Danuser, G. (2002). Automatic fluorescent tag detection in 3D with super-resolution: application to the analysis of chromosome movement. *J. Microsc.* **208**, 49-64.

Treanor, B., Depoil, D., Gonzalez-Granja, A., Barral, P., Weber, M., Dushek, O., Bruckbauer, A. and Batista, F. D. (2010). The membrane skeleton controls diffusion dynamics and signaling through the B cell receptor. *Immunity* **32**, 187-199.

Veatch, S. L., Chiang, E. N., Sengupta, P., Holowka, D. A. and Baird, B. A. (2012). Quantitative nanoscale analysis of IgE-FcepsilonRI clustering and coupling to early signaling proteins. *J. Phys. Chem. B* **116**, 6923-6935.

Volpert, O. V., Zaichuk, T., Zhou, W., Reiher, F., Ferguson, T. A., Stuart, P. M., Amin, M. and Bouck, N. P. (2002). Inducer-stimulated Fas targets activated endothelium for destruction by anti-angiogenic thrombospondin-1 and pigment epithelium–derived factor. *Nat. Med.* **8**, 349-357.

Williamson, D. J., Owen, D. M., Rossy, J., Magenau, A., Wehrmann, M., Gooding, J. J. and Gaus, K. (2011). Pre-existing clusters of the adaptor lat do not participate in early T cell signaling events. *Nat. Immunol.* **12**, 655-662.